ACS MATERIALS Au
AN OPEN ACCESS JOURNAL OF THE AMERICAN CHEMICAL SOCIETY

pubs.acs.org/materialsau Article

On the Interplay Between Oxygen Vacancies and Small Polarons in Manganese Iron Spinel Oxides

Roni Eppstein and Maytal Caspary Toroker*

Cite This: ACS Mater. Au 2022, 2, 269–277

Read Online

ACCESS | Metrics & More | Article Recommendations | Supporting Information

ABSTRACT: Ternary spinel oxides are promising materials due to their potentially versatile properties resulting from the disorder inherent in their crystal structure. To fully unlock the potential of these materials, a deeper understanding of their electronic structures, both as pristine and defective crystals, is required. In the present work, we investigate the effects of oxygen vacancies on the electronic structure and charge transport properties of the ternary spinel oxide $Mn_xFe_{3-x}O_4$, modeled on epitaxial thin films of the material, using density functional theory + U (DFT + U). The formation energy of a single oxygen vacancy in the spinel cell is found to be large and unaffected by changes in stoichiometry, in agreement with experimental results. We find that the immediate vicinity of the vacancy has a marked impact on the formation energy. In particular, Mn cations are found to be preferred over Fe as sites for charge localization around the vacancy. Finally, we examine the charge transport in the defective cell using the formalism of Marcus theory and find that the activation barrier for electron small-polaron hopping between sites not adjacent to the vacancy is significantly increased, with a large driving force toward sites that reside on the same (001) plane as the vacancy. Hence, vacancies delay charge transport by increasing the activation barrier, attributed to a rearrangement of vacancy-released charge on the cations immediately neighboring the vacancy site. These results highlight the impact of oxygen vacancies on charge transport in spinel oxides.

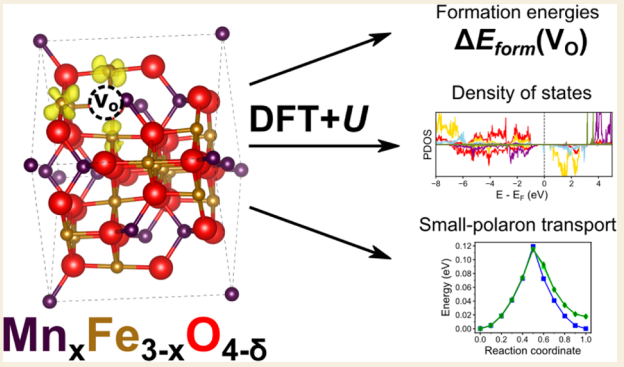

KEYWORDS: *spinels, oxygen vacancies, small-polaron transport, manganese iron oxide spinel, density functional theory, charge transport*

INTRODUCTION

Oxide materials have been utilized in a wide array of applications, ranging from photovoltaics[1−3] to fuel cells[4−6] and electronic[7−9] and spintronic[10,11] devices, whose efficiency relies on the electronic conductivity of the oxides. Charge carrier dynamics in oxide materials is often described by small-polaron theory,[12,13] where carriers are trapped on specific sites due to their interaction with the lattice atoms and their phonons (leading to the term "self-trapping"). The self-trapped carrier can propagate through the lattice either by tunneling (nonadiabatically) or hopping (adiabatically) between pairs of trapping sites.[14] The transport of small polarons in these systems has been found to be dependent on the type of hopping pairs in the material,[15,16] allowing the electronic properties to be tuned through control of the cation disorder in the system.[17]

It is widely known that point defects, in particular oxygen vacancies, can have significant effects on the electronic and electrochemical properties of oxides.[18] For example, in hematite (α-Fe_2O_3), it has been recently reported that oxygen vacancies enhance the catalytic performance at the (110) facet.[19] In wüstite (FeO), the effects of both oxygen[20] and iron[21] vacancies on small-polaron transport have been studied theoretically. Studies on (doped and undoped) hercynite ($FeAl_2O_4$) have shown that the cation configuration around the oxygen vacancy has a large impact on its formation energy and its transport kinetics.[22,23] Oxygen deficiency has also been reported to improve the performance of spinel cathodes in Li-ion batteries[24] as well as of spinel catalysts for the oxygen evolution reaction.[25]

In our recent work,[16] we reported that charge transport in $Mn_xFe_{3-x}O_4$ (MFO) is highly dependent on stoichiometry (i.e., the value of "x"). In particular, it was shown both experimentally and theoretically that the trends in conductivity can be explained by a decoupling of transport pathways, based on the elemental pairs (Fe^{2+}/Fe^{3+} or Mn^{2+}/Mn^{3+}) participating in electron small-polaron hopping. The presence of oxygen vacancies in MFO has been observed experimentally through X-ray photoemission spectroscopy (XPS),[16] where their

Received: September 25, 2021
Revised: December 1, 2021
Accepted: January 12, 2022
Published: January 27, 2022

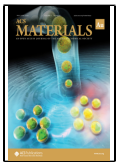

https://doi.org/10.1021/acsmaterialsau.1c00051
ACS Mater. Au 2022, 2, 269–277

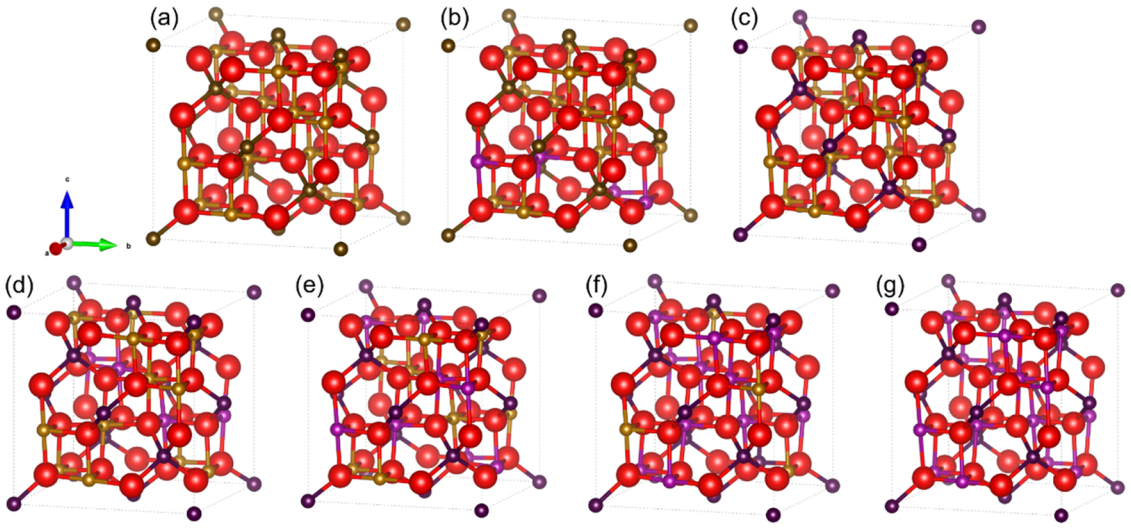

Figure 1. Epitaxially strained $Mn_xFe_{3-x}O_4$ (MFO) spinel system. Tetrahedral (T_d, dark) and octahedral (O_h, light) cations are shown as golden (Fe) and magenta (Mn) spheres, while oxygen anions are shown in red. (a) Inverse Fe_3O_4 (x = 0, $Fe_{24}O_{32}$). (b) Inverse $Mn_{0.5}Fe_{1.5}O_4$ (x = 0.5, $Mn_4Fe_{20}O_{32}$). (c) Normal $MnFe_2O_4$ (x = 1, $Mn_8Fe_{16}O_{32}$). (d) Normal $Mn_{1.5}Fe_{1.5}O_4$ (x = 1.5, $Mn_{12}Fe_{12}O_{32}$). (e) Normal Mn_2FeO_4 (x = 2, $Mn_{16}Fe_8O_{32}$). (f) Normal $Mn_{2.5}Fe_{0.5}O_4$ (x = 2.5, $Mn_{20}Fe_4O_{32}$). (g) Normal Mn_3O_4 (x = 3, $Mn_{24}O_{32}$). Crystal structures are visualized using VESTA.[34]

concentrations were found to be relatively uniform across the stoichiometric range. However, the impact of oxygen vacancies on MFO, in particular in relation to the transport properties, is unclear. Elucidating the role of oxygen vacancies in the transport properties of spinel oxides can provide new approaches and insights for tuning these materials for specific applications.

In this paper, we computationally examine the energetics and effects of oxygen vacancies on both the electronic structure and transport properties of MFO. In particular, we report the calculated oxygen vacancy formation energies as well as the activation barriers and driving forces for small-polaron transport in the oxygen-deficient cells.

METHODS

Spin-resolved density functional theory[26,27] (DFT) calculations were performed using the Vienna *Ab initio* Simulation Package (VASP, version 5.4.4), utilizing the Perdew–Burke–Ernzerhof (PBE) generalized gradient approximation for the exchange–correlation functional,[28] with core electrons replaced by projector-augmented wave (PAW) pseudopotentials.[29,30] Fe, Mn, and O, respectively, contributed 8, 7, and 6 valence electrons. On-site Coulomb corrections were introduced for Fe and Mn 3d electrons by adding a Hubbard U_{eff} parameter.[31] The Hubbard terms $U_{eff} = U-J$ used in this study were 3.61 and 3.3 eV for Fe and Mn, consistent with values used in previous work on manganese and iron oxides, respectively.[32,33]

The modeled systems are all 56-atom strained $Mn_xFe_{3-x}O_4$ cells (Figure 1), derived from experimental epitaxial thin-film samples (grown on a MgO(001) substrate),[16] where the two in-plane (IP, with respect to the substrate) lattice parameters are fixed at $a = b$ = 8.434 Å, corresponding to (twice) the MgO substrate's lattice constant, and the out-of-plane (OOP) lattice parameter (c) increases in value as x is increased, from $c(Fe_3O_4)$ = 8.356 Å to $c(Mn_3O_4)$ = 9.431 Å, resulting in a stronger tetragonal distortion of the cells as the Mn content increases, which is also observed in bulk samples.[35] The lattice parameters are kept constant (for each cell) throughout the calculations, with the exception of calculations in x = 1 and 2, where all of the lattice parameters are allowed to relax to examine the impact of cell volume on the calculations. In all cases, the cells are ferrimagnetically ordered such that the cations occupying the O_h sublattice are parallel to each other (spin up) and antiparallel to the cations in the T_d sublattice (spin down), following the collinear Néel model.[36] The ferrimagnetic ordering has been previously reported for Fe_3O_4,[37] $MnFe_2O_4$,[32,38−40] and Mn_2FeO_4.[41] Defective cells are created by removing a single oxygen anion from the relaxed 56-atom cell, thus forming $Mn_xFe_{3-x}O_{3.875}$ (an oxygen deficiency of δ = 0.125) and subsequently relaxing the internal positions of the ions, while fixing the volume and shape of cells. The cells at stoichiometries of x = 0 and 0.5 are completely inverse spinels, with T_d sites all occupied by Fe^{3+} cations, while the remaining cells are all normal spinels (with Mn^{2+} in T_d sites), chosen to correspond with both the experimental and theoretical results on the preference for inversion detailed in our previous work as well as previous reports.[16,42,43]

Calculations were performed with a cutoff energy of 600 eV. A Γ-point centered 4 × 4 × 4 k-point mesh was used for ionic relaxations and polaron transport calculations, with a denser 6 × 6 × 6 mesh employed for density of states and defect formation energy calculations. The cutoff energy and k-point mesh were tested for convergence of the total energy to 1 meV/atom. Electronic relaxations were performed until a convergence threshold of 0.1 meV was reached. The ionic relaxation convergence threshold was set at a maximal force value of 0.01 eV/Å. Bader charge analysis[44] was performed using the code developed by the Henkelman group.[45−48]

Oxygen vacancy formation energies ΔE_{form} were calculated as follows:

$$\Delta E_{form} = E_0^{vac} + \frac{1}{2}E_{O_2} - E_0 \quad (1)$$

where E_0 and E_0^{vac} are the total energies of the pristine and defective cells (after the internal positions of the ions were relaxed), respectively, and E_{O_2} = −9.873 eV is the total energy of an O_2 molecule in vacuum (after relaxation of the bond length). No distortion was applied to the cells with the oxygen vacancy prior to relaxation. To ensure that the energy of the O_2 molecule is not affected by molecules in neighboring (periodic) unit cells, the volume of the cell was kept fixed at 15 × 15 × 15 Å^3. Since in the calculation of the vacancy formation energy (eq 1) half of the total energy of the oxygen molecule is added, any inaccuracy will be applied to all of the formation energies and thus will not impact the comparative analysis. With the exception of transport calculations with excess (localized) charge in the cell, all defective cells were electrically neutral.

We employ the formalism of Marcus theory for electronic processes in chemical reactions,[49−51] wherein the initial and final polaron states are represented by nonadiabatic (or diabatic) energy surfaces. In

https://doi.org/10.1021/acsmaterialsau.1c00051
ACS Mater. Au 2022, 2, 269−277

practice, generating Marcus theory curves is done by localizing a single excess electron on an initial site and subsequently on a neighboring (final) site. In the same manner used in our previous study,[16] this was accomplished by initially distorting the bonds around the chosen site[52] by 8% and increasing the U_{eff} value by 2 eV for all of the metal ions.[51] U_{eff} was increased uniformly so that the effects on the cations could be comparable between stoichiometries. The bond distortion creates an initial trap for the excess electron, while the increased U_{eff} value ensures that the charge remains localized throughout the transport process and allows a comparison with our previous results on pristine $Mn_xFe_{3-x}O_4$.[16] While the increase in U_{eff} is well known to lead to an increase in the band gap of the neutral material, for the present work the increase in the parameter is used for the purpose of ensuring charge localization, in particular at nonequilibrium geometries. The structure was then allowed to relax (both electronically and ionically) and the localization was verified by examining the magnetic moment and effective (Bader[44]) charge on the chosen site, both of which should correspond to a reduction of the oxidation state.

Following the charge localization procedure, transport reaction geometries were generated by linear interpolation of the geometries,[21,51] according to

$$\mathbf{r}(q) = (1 - q)\mathbf{r}(0) + q\mathbf{r}(1) \quad (2)$$

where $\mathbf{r}(q)$ is the position vector at reaction coordinate q. For each interpolated cell geometry, a single-point (fixed geometry) calculation was performed to account for the energy needed for charge transport accompanied by a geometrical change along the reaction coordinate q. The energy difference $\Delta E(q) = E_0(q) - \min(E_0(0), E_0(1))$ was then computed. The resulting $\Delta E(q)$ curve could be described using Marcus theory, from which we extracted the activation barrier and driving force for charge transport. The converged wavefunctions from nearby reaction coordinates q were used as the initial guess for subsequent calculations. In the present study, we also performed a similar procedure in the oxygen-deficient cells without the addition of an excess electron, allowing for strong localization of charge released by the vacancy onto different vacancy-neighboring octahedral sites. Localization of charge on a particular cation adjacent to the vacancy was achieved by initially distorting the M−O (M = Fe/Mn) bonds around a site located away from the vacancy.

RESULTS

In this section, we present the results of calculations of oxygen vacancy formation energies and their dependence on stoichiometry in the MFO system. In addition, we detail the changes in atomic magnetic moments, effective charges, and their relation to stoichiometry and cation configuration. We find that while formation energies are relatively constant throughout the stoichiometric range in MFO (Figure 2a), they depend both on the local configuration and the symmetry of the cells. Finally, we examine how the oxygen vacancy affects the transport of charge both around the vacancy and away from it when excess charge is introduced into the cell.

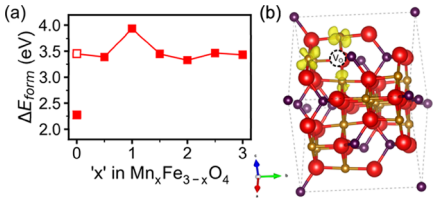

Figure 2. (a) Oxygen vacancy formation energy ΔE_{form} as a function of x. For $x = 0$ (Fe_3O_4), the results differ significantly between the symmetry-constrained case (filled square) and the nonconstrained case (empty square). (b) Charge density difference for the $x = 1$ case ($MnFe_2O_4$) with an oxygen vacancy relative to the pristine cell. Positive charge density differences are shown as yellow isosurfaces.

Oxygen Vacancy Formation Energies

Oxygen vacancy formation energies, calculated according to eq 1, are nearly constant across all MFO cells tested (Figure 2a and Table 1), consistent with the uniform concentration of oxygen vacancies throughout the stoichiometric range, observed in X-ray photoemission spectroscopy measurements of the epitaxial thin films.[16] We note that while the formation energy is large, ∼3.5 eV (Figure 2a and Table 1), it is consistent both with reports for other spinels[22,53−57] and iron oxides.[19,58,59]

At stoichiometries of $x = 1$ and 2, the vacancy formation energies are also calculated in cells where the shape and volume of the cell as well as the internal positions of the ions are allowed to relax before and after oxygen removal (see items marked with superscript "c" in Table 1) and the formation energies (3.98 and 3.50 eV for $x = 1$ and 2, respectively) show little deviation from those found for the epitaxial cells (3.93 and 3.33 eV), while the distances between the vacancy sites and neighboring cations are markedly different (Table S1), implying that cell shape is not a determining factor for the vacancy formation energy likely because of the strong localization of charge around the vacancy. All of the results that follow in this work are for the strained cells, based on the experimental thin-film samples, unless stated otherwise. Fixing the cells at these geometries allows for a more apt comparison with the experimental results obtained for MFO thin films.[16]

For the magnetite cells ($x = 0$, Fe_3O_4), the results differ significantly between the cells obtained when enabling or disabling symmetry constraints from the VASP calculations, with the unconstrained cell result falling in line with the results at other stoichiometries (Figure 2a, empty square) and with previously reported GGA + U results,[57] while the symmetry-constrained cell is markedly lower and consistent with a value previously reported in the literature.[60] The decreased formation energy for the symmetry-constrained case is the result of a significantly higher total energy for the pristine cell (−387.38 eV) as compared to the nonconstrained case (−388.67 eV). The difference in energies between the symmetry-constrained and unconstrained cells is attributed to the energetically favored (at $T = 0$ K) insulating state obtained in the symmetry-unconstrained calculation instead of the half-metallic state obtained when symmetry is enforced in the calculations. The oxygen-deficient cells have similar energies (−380.16 and −380.28 eV) as the removal of the oxygen ion breaks the symmetry sufficiently to result in similar states in both cases, following relaxation.

The largest formation energy is observed for the $x = 1$ cell ($MnFe_2O_4$, Figure 2b), implying a dependence of the vacancy formation energy on the type of cation surrounding the vacancy site. This unit cell is unique among the cells in that it is populated exclusively by Fe^{3+} and Mn^{2+} cations in the O_h and T_d sublattices, respectively. In contrast, the inverse magnetite cell ($x = 0$) has Fe^{3+} cations in the T_d sublattice, while the O_h sublattice is comprised of Fe^{2+} and Fe^{3+} cations, in the symmetry-unconstrained cell. For cells at $x > 1$, Mn cations are added to the O_h sublattice and have a formal oxidation state of 3+ (in the pristine cell). This implies that, for the normal spinel, the octahedral Mn^{3+} cations reduce the vacancy formation energy, as will be expanded on below. Examining the changes (as compared to the pristine cells) in

https://doi.org/10.1021/acsmaterialsau.1c00051
ACS Mater. Au 2022, 2, 269−277

Table 1. Oxygen Vacancy Formation Energy (ΔE_{form}) and Differences in Magnetic Moment ($\Delta\mu$) and Effective (Bader) Charge (ΔQ) for MFO Cells[a]

		$\Delta\mu$ (μ_B)				ΔQ (|e|)			
x in $Mn_xFe_{3-x}O_4$	ΔE_{form} (eV)	IP		OOP	T_d	IP		OOP	T_d
0	2.28	−0.35[d]	−0.36[d]	−0.14[d]	0.45[d]	−0.25[d]	−0.25[d]	−0.23[d]	−0.38[d]
	3.45[b]	−0.15[d]	−0.23[d]	−0.06[d]	0.44[d]	−0.20[d]	−0.30[d]	−0.16[d]	−0.38[d]
0.5	3.39	−0.06[d]	−0.05[d]	−0.38[d]	0.43[d]	−0.10[d]	−0.09[d]	−0.37[d]	−0.39[d]
1	3.93	−0.29[d]	−0.28[d]	−0.24[d]	−0.08	−0.24[d]	−0.24[d]	−0.29[d]	−0.11
	3.98[c]	−0.24[d]	−0.17[d]	−0.25[d]	−0.05	−0.20[d]	−0.20[d]	−0.20[d]	−0.09
1.5[e]	3.45	−0.54[d]	−0.22[d]	−0.14	−0.11	−0.41[d]	−0.29[d]	−0.16	−0.15
2	3.33	−0.25[d]	0.67	−0.10	−0.03	−0.36[d]	−0.33	−0.15	−0.14
	3.50[c]	0.68	−0.35[d]	−0.05	−0.01	−0.32	−0.35[d]	−0.10	−0.09
2.5	3.47	0.64	−0.08	−0.31[d]	0.00	−0.30	−0.13	−0.36[d]	−0.11
3	3.43	0.63	0.63	0.01	0.03	−0.29	−0.29	−0.08	−0.05

[a]IP and OOP refer to cations in-plane and out-of-plane (with respect to the (001) plane) with the vacancy, respectively. [b]No symmetry constraints. [c]Relaxed cell shape and volume before and after oxygen removal. [d]Fe cation. [e]Changing the arrangement of cations around the vacancy allows a lower formation energy (3.30 eV); see Table 2.

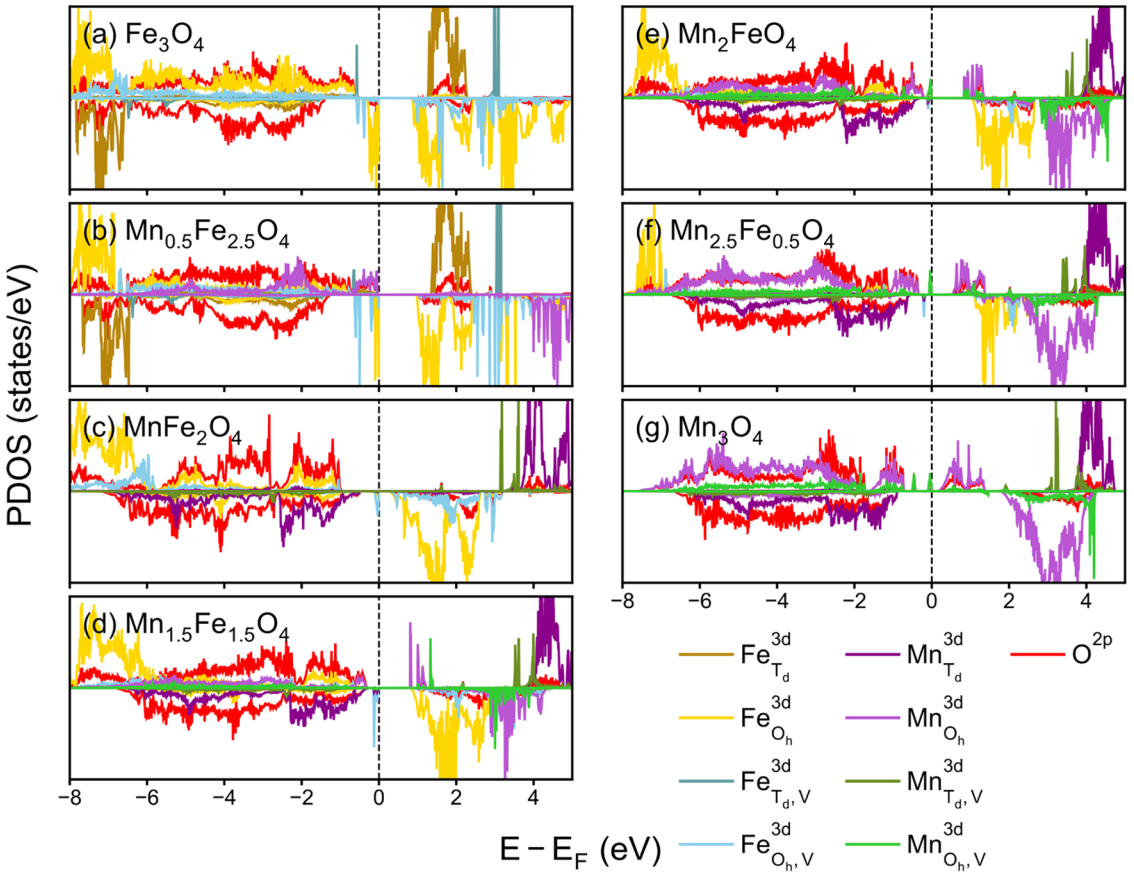

Figure 3. (a–g) Spin-resolved projected density of states (PDOS) for the oxygen-deficient cells between x = 0 (a) and x = 3 (g). All results are aligned at the Fermi level. States labeled with subscript "V" (for example, $Fe^{3d}_{O_h,V}$) refer to cations that are adjacent to an oxygen vacancy.

atomic magnetization, effective (Bader) charges (Table 1), metal-vacancy distances, and the metal–oxygen bond lengths in the defective cells (Table S1), we find that charge released by the vacancy localizes near the vacancy, on the formerly 3+ cations. The differences in the atomic magnetizations and effective charges are calculated as $\Delta X = X_{vac} - X_0$ ($X = \mu, Q$), where the subscripts "vac" and "0" refer to the oxygen-deficient and pristine cells, respectively. While in general changes in atomic magnetization and effective (Bader) charge give a strong indication for changes in the oxidation state, they can slightly differ (for example, in the x = 2.5 cell, the T_d cation's magnetic moment is unchanged, whereas its effective charge is reduced by 0.11 |e|), consistent with previous literature on oxides[61] and as can be seen in Table 1.

In the inverse spinels (x = 0, 0.5), charge released by the vacancy localizes on the surrounding (formerly) Fe^{3+} cations, both in O_h and T_d sites, reducing them from Fe^{3+} to Fe^{2+}. For the symmetry-constrained magnetite cell, the vacancy induces charge separation across the O_h sublattice in the cell (into distinct Fe^{3+} and Fe^{2+} states), in contrast to the delocalized states (i.e., the intermediate $Fe^{2.5+}$ oxidation state) seen in the pristine cell that does not include a vacancy. Conversely, in the

https://doi.org/10.1021/acsmaterialsau.1c00051
ACS Mater. Au 2022, 2, 269–277

nonconstrained magnetite cell, we see no major changes to magnetization or effective charge away from the vacancy's immediate vicinity as a result of excess electrons induced by vacancy formation, as the octahedral Fe cations were already split into distinct Fe^{2+} and Fe^{3+} states before the vacancy was formed, consistent with previous reports on the effects of symmetry constraints in magnetite.[62]

For the normal spinel cells ($x \geq 1$), localization is limited to the O_h sublattice, with the tetrahedral Mn^{2+} showing only minor changes in effective charge and negligible changes in atomic magnetization. This can be explained by the fact that unoccupied tetrahedral Mn states are much higher in energy, as is detailed later in the projected density of states analysis. From the positive charge density difference (i.e., the additional charge left by the vacancy) in the $x = 1$ cell (Figure 2b), it can be seen that the charge localizes equally on the octahedral neighbors' 3d orbitals. We note that charge transport calculations in cells without an excess charge, detailed later in the text, show that distorting the lattice (and increasing the U_{eff} value) can lead to nonsymmetric charge localization around the vacancy.

Localization on the in-plane (IP, located on the same (001) plane as the vacancy) Mn cations appears to be energetically preferred, as we see no localization on the out-of-plane (OOP, located along the [001] direction from the vacancy) Mn cation. For the Fe neighbors, the preference for localization on IP cations is less pronounced, as there are OOP Fe cations that hold a significant amount of charge, in particular, for the $x = 0.5$ and 2.5 cells.

In the $x = 0.5$ cell, the charge is primarily localized on the OOP ($\Delta Q = -0.37$ |e|) and T_d ($\Delta Q = -0.39$ |e|) Fe cations. Since in the examined cell the two octahedral Fe cations sharing the (001) plane (IP sites) with the vacancy are originally in the 2+ oxidation state, a reduction of the oxidation state would incur a significant energetic cost. Additionally, the $x = 0.5$ cell is nearly cubic ($c/a \approx 1.001$), meaning that the elongation of the Fe−O bond along the [001] direction is expected to be equivalent to that along the perpendicular directions.

For the $x = 2.5$ case, the charge is localized mainly on an IP Mn cation ($\Delta Q = -0.30$ |e|) and on the OOP Fe cation ($\Delta Q = -0.36$ |e|). We explain this apparent deviation from the overall preference for the IP cations by considering the following. First, the cell is significantly distorted ($c/a \approx 1.052$) and the 5.4% elongation of the Fe−O bond, resulting from the localization of vacancy-released charge, in the OOP direction is concomitant with the overall tetragonal distortion of the cell. Second, since the Mn^{3+} cations exhibit Jahn−Teller deformation, the OOP Mn^{3+} is located farther away from the vacancy site than the IP cations (Table S1). Consider the $x = 1.5$ cell where the Fe−vacancy distance (along the IP directions) is on average 2.00 Å, while the OOP Mn cation is at a distance of 2.18 Å. On the other hand, in the $x = 2.5$ cell, the IP cations (Fe and Mn) are located at an average distance of 2.04 Å and the OOP Fe−O distance is 2.06 Å. We note that in any of the cells where the OOP cation is a Mn^{3+} cation prior to oxygen removal ($x = 1.5$, 2, and 3), the cation is not observed to be the primary charge-holding site after the oxygen is removed.

Spin-resolved projected density of states (Figure 3) analysis shows narrow trap-like states in the vicinity of the Fermi energy, associated with cations around the vacancy. The projected density of states for pristine $Mn_xFe_{3-x}O_4$ is given in our previous work.[16] The density of states is projected on the ions around the vacancy (blue and green lines in Figure 3), with the remaining cations' states projected according to their sublattice (i.e., O_h or T_d). Generally, in the inverse spinels ($x = 0$, 0.5, Figure 3a,b), the oxygen vacancy leads to states below the valence band maximum (VBM), whereas for the normal spinels ($x \geq 1$), the states associated with the vacancy-neighboring ions are located inside a gap formed by the ions that are not adjacent to the vacancy, which is attributed to the band gap of the pristine material.[16] For the magnetite cell, we see that both the T_d and O_h cations around the vacancy form sharp peaks below the VBM (Figure 3a, blue lines), while no vacancy-induced states are seen inside the band gap. In the $x = 1$ cell, we observe the vacancy-induced states forming inside the band gap (Figure 3c, light blue lines), associated primarily with the octahedral Fe cations located near the vacancy. In-gap states are also seen for the $x = 2$ cell, here associated with both octahedral Fe (spin down) and Mn (spin up) cations and located closer to the VBM (Figure 3e, light blue and green lines). In Mn_3O_4, two trap states are formed inside the band gap, one near the conduction band minimum and the second lower in energy and near the VBM (Figure 3g, light green lines). For the normal cells ($x \geq 1$), no states close to the Fermi level are associated with the tetrahedral cations, in contrast to the results for the inverse spinels. In all cases, the resulting states associated with cations near the vacancy are highly localized, indicated by their sharpness in the density of states plots.

The vacancy formation energy increases with the number of Fe nearest neighbors, as shown for the normal $x = 1.5$ cell (Figure 4, Table 2, and Figure S1). The formation energy

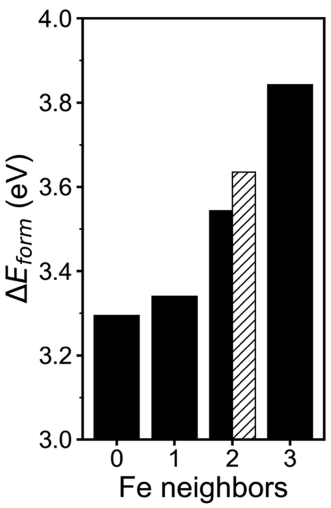

Figure 4. Oxygen vacancy formation energy as a function of the number of Fe neighbors (in O_h sites) in the normal $x = 1.5$ cell, with the remaining cations being Mn. For two Fe neighbors, the solid bar is the configuration where one of the in-plane neighbors is Mn, while the slash-hatched bar is the configuration where the two in-plane neighbors are Fe.

obtained with three O_h Fe neighbors around the vacancy site (the fourth neighbor being the T_d Mn^{2+} cation) in the $x = 1.5$ cell (3.84 eV) is consistent with the value found in the $x = 1$ cell, where all O_h neighbors around the vacancy are Fe, implying that the reason for the large formation energy in the $x = 1$ cell (3.93 eV, Figure 2a) is indeed the number of O_h Fe

https://doi.org/10.1021/acsmaterialsau.1c00051
ACS Mater. Au 2022, 2, 269−277

Table 2. Oxygen Vacancy Formation Energy (ΔE_{form}) and Differences in Magnetic Moment ($\Delta\mu$) and Effective (Bader) Charge (ΔQ) for Different Configurations of Neighbors Around the Oxygen Vacancy at $x = 1.5$[a]

		$\Delta\mu$ (μ_B)				ΔQ (|e|)			
Fe neighbors	ΔE_{form} (eV)	IP		OOP	T_d	IP		OOP	T_d
0	3.30	−0.16	0.67	−0.14	−0.10	−0.22	−0.40	−0.17	−0.23
1	3.34	0.67	−0.09	−0.24[b]	−0.03	−0.37	−0.15	−0.33[b]	−0.14
2	3.55	−0.17[b]	0.67	−0.16[b]	−0.04	−0.23[b]	−0.36	−0.20[b]	−0.14
2	3.64	−0.23[b]	−0.54[b]	−0.12	−0.09	−0.30[b]	−0.46[b]	−0.15	−0.15
3	3.84	−0.15[b]	−0.54[b]	−0.19[b]	−0.06	−0.19[b]	−0.44[b]	−0.26[b]	−0.12

[a]IP and OOP refer to cations in-plane and out-of-plane (with respect to the (001) plane) with the vacancy, respectively. [b]Fe cation.

cations neighboring the vacancy site. The stoichiometry of the cell is maintained at $x = 1.5$ (Figure S1) throughout the calculations (i.e., each cell has 12 Mn and 12 Fe cations, with a different arrangement). Due to the highly localized nature of the vacancy-induced charge ordering observed in this work, we expect the results to be qualitatively applicable for other stoichiometries.

In general, we find that the charge preferentially localizes on one of the IP neighbors (on the (001) plane with the vacancy), with the OOP neighbor and the tetrahedral site holding a smaller amount of charge in comparison, as seen in the changes in atomic magnetizations and effective charges (Table 2). For example, in the case of a single Fe neighbor around the vacancy, one of the IP Mn cations sees the largest changes in magnetization ($\Delta\mu = 0.67\ \mu_B$) and effective charge ($\Delta Q = -0.37$ |e|). Comparing the cases where the vacancy has two Fe neighbors and two Mn neighbors (both formerly T_d and O_h), we see that the formation energy is higher if both Fe cations are located on the IP sites (3.64 eV, slash-hatched bar in Figure 4 and Table 2), in comparison with the case where the IP cations are Fe and Mn (3.55 eV), and the charge localizes primarily on the Mn cation. This preferential localization on Mn has been observed for other oxides[63] as well as in the epitaxial MFO system in the context of small-polaron formation.[16] This result is likely due to larger energy gain when forming a Mn^{2+} cation, as compared with the formation of an Fe^{2+} cation—both in terms of ionization potentials and exchange interactions between like-spin electrons on the cations. We would thus expect to see more Mn-coordinated oxygen vacancies (with the charge-holding Mn cations located on the same (001) plane as the vacancy).

Transport in Defective Cells

Transport calculations near the vacancy in the normal $x = 1$ ($MnFe_2O_4$) cell show that charge localized on an Fe cation near the vacancy (Figure 5a, blue and green arrows) can transport to other vacancy-neighboring cations with a low activation energy (~0.12 eV as seen in the energy barrier of Figure 5b), as compared with transport of excess charge in the pristine, undefective cell (~0.24 eV).[16] We note that charge transport calculations are limited to octahedral cation pairs, as formation of tetrahedral Mn^{3+} cations requires a significant increase in the total energy, as detailed in our previous work.[16] Transport between the cations on IP sites (labeled NV_{IP1} and NV_{IP2} in Figure 5a) results, as expected, in a symmetrical Marcus curve (Figure 5b, blue) as these are symmetrically equivalent states. Charge localized on the IP cations results in magnetic moments of 3.75 and 4.18 μ_B ($\Delta\mu = -0.43\ \mu_B$) and effective charges of 1.22 |e| and 1.48 |e| ($\Delta Q = -0.26$ |e|), on the donor and acceptor states, respectively, indicating that distorting the bonds and increasing the U_{eff} value produces a

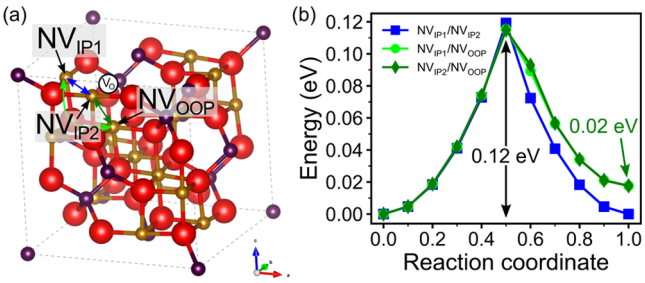

Figure 5. (a) Defective $x = 1$ cell. Near-vacancy transport pairs (NV_{IP1}, NV_{IP2}, and NV_{OOP}) are marked by blue (in-plane, IP) and green (out-of-plane, OOP) arrows. The oxygen vacancy site is marked by the empty black circle. (b) Marcus theory curves for the near-vacancy transport.

state with nonsymmetric localization around the vacancy. Charge localized on the OOP cation (NV_{OOP}) leads to magnetic moments of 3.75 and 4.19 μ_B ($\Delta\mu = -0.44\ \mu_B$) and effective charges of 1.23 |e| and 1.49 |e| ($\Delta Q = -0.26$ |e|), for the donor and acceptor states, respectively. Transport between the IP and OOP ($NV_{IP1} \leftrightarrow NV_{OOP}$ and $NV_{IP2} \leftrightarrow NV_{OOP}$) sites neighboring the vacancy shows a small driving force of ~0.02 eV, with the IP sites favored energetically (Figure 5b, light and dark green). The driving forces for transport between the IP and OOP sites are attributed to the fact that these sites are not symmetrically equivalent since the cell is tetragonally deformed. In all cases, the resulting curves are quadratic, and the charge is localized on either of the endpoint sites, both characteristics of nonadiabatic Marcus curves.

The near-vacancy transport results imply that inducing a large amount of oxygen vacancies could have a twofold effect on conductivity in the material. First, increasing the oxygen vacancy content leads to an increase in the number of excess charge carriers, as each vacancy releases its two electrons to the nearby cations, forming more Fe^{2+} cations. Second, transport of charge localized around the vacancy has a lower activation energy, as compared to transport between pairs in the pristine bulk. While both of these points may improve the conductivity of the material, they rely on the formation of a network of vacancies, and there is no indication of how the vacancy will affect charge transport between cations that do not neighbor it directly.

When excess charge is transported between sites that are not immediately adjacent to the vacancy (Figure 6), the activation barrier for transport is increased (~0.36 eV), as compared with transport in the pristine $x = 1$ cell (~0.24 eV).[16] The results for Fe/Fe transport in the pristine cells, as reported in our previous paper, are relatively constant throughout the stoichiometric range and exhibit the same nonadiabatic character as those seen in Figure 6b. To examine the effect

https://doi.org/10.1021/acsmaterialsau.1c00051
ACS Mater. Au 2022, 2, 269−277

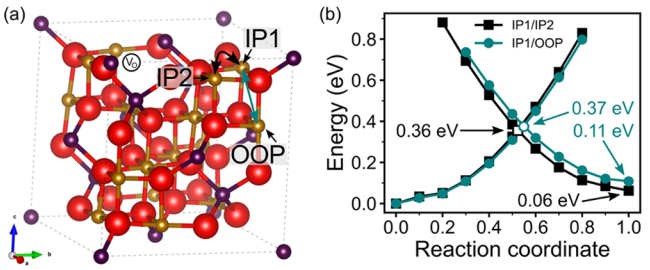

Figure 6. (a) Defective $x = 1$ cell with the excess charge transport pairs (IP1, IP2, and OOP) marked by black (in-plane, IP) and teal (out-of-plane, OOP) arrows. The oxygen vacancy site is marked by the empty black circle. (b) Marcus theory curves for transport of excess charge in the oxygen-deficient cell. The empty markers mark the intersection of the curves, which is the nonadiabatic activation energy.

of the vacancy on excess charge transport, charge was localized on a set of three sites (Figure 6a), two of which are in equivalent positions relative to the vacancy (IP1 and IP2, black double-headed arrow in Figure 6a) and the third out of the (001) plane of the vacancy (OOP). Transport curves were then calculated for the two pairs indicated by the black and teal arrows in Figure 6a. Transport between the sites that are symmetrical with regard to the vacancy (Figure 6b, black) results in a large barrier (0.36 eV, the intersection of the two quadratic curves) as well as a small driving force (0.06 eV). The activation energy for hopping between nonsymmetrical sites (Figure 6b, teal) is slightly larger still (0.37 eV) with nearly twice the driving force (0.11 eV). The larger driving force is likely the result of the OOP cation being farther away from the vacancy site (at a distance of 6.18 Å from the position of the removed oxygen in the pristine cell) as compared with the IP cations (4.68 Å), implying that the electrons are driven toward the vacancy site. In both cases, the excess electron is strongly localized at either the initial or final site throughout the transport process, indicating that the resulting quadratic curves are characteristic of nonadiabatic transport, providing an upper bound for adiabatic (hopping) transport.

The localization of excess charge away from the vacancy leads to a rearrangement of the charge adjacent to the vacancy, in such a way that the localized electrons, both the excess electron and the charge donated by the vacancy, are located at the maximal distance from one another (Tables S2 and S3). For example, when an excess charge is localized on IP1, the vacancy-induced charge is predominantly localized on the NV_{IP2} site located at a maximal distance of 5.96 Å (Table S2) from IP1. The resulting intermediate geometries therefore have simultaneous transformation of the geometry around the transport pair (far from the vacancy) as well as around the vacancy. This result indicates that the elevated activation energies are the outcome of a convolution of two transport events: the excess charge transport and the transport of charge localized around the vacancy. Indeed, summing the activation energy of transport in the pristine cell ($E_{a,p} = 0.242$ eV)[16] with the (averaged) activation energy for charge transport near the vacancy ($\langle E_{a,V_O} \rangle = 0.117$ eV) leads to a value of 0.359 eV, nearly identical to the activation energy obtained from the first-principles calculations for transport of excess charge in the defective cell. Therefore, we hypothesize that charge transport far from the vacancy should not be affected by the vacancy, provided that it is sufficiently distant so that the excess charge cannot interact with the charge localized around the vacancy.

The charge transport calculation results imply that controlling oxygen content could provide another meaningful avenue for tuning the transport properties of MFO, with more intricate outcomes than simply increasing the charge carrier concentration through the release of electrons onto the metal cation networks. Since transport between cations that are nearest neighbors to the vacancy is markedly lower in activation energy, the formation of percolation pathways that connect the vacancies through metal cations could result in a better conducting material. Additionally, since the charge preferentially localizes on and transports between in-plane cations in the epitaxial cells, the introduction of oxygen vacancies can produce an inherent anisotropy for charge transport. In contrast, for cases where excess charge is transported through a material, creating oxygen vacancies could hinder transport, increasing resistivity, by forcing a dual transport process where the charge around the vacancy must accommodate the movement of charge farther away from the vacancy.

CONCLUSIONS

In summary, we examined the effect of stoichiometry on the oxygen vacancy formation energy in epitaxial cells of $Mn_xFe_{3-x}O_4$ and found it to be nearly constant for values of $x > 0$ at ~3.5 eV, in agreement with the uniform vacancy concentration seen in XPS measurements.[16] Charge localization around the vacancy is markedly different for the inverse and normal spinels, with the tetrahedral Fe^{3+} reducing to Fe^{2+} for the former, while only the octahedral (Mn and Fe) sites are involved for the latter. Additionally, it was found that the charge preferentially localized on the in-plane Mn cations around the vacancy site. We found that the oxygen vacancy formation energy increases as the number of Fe cations neighboring the vacancy site is increased, indicating that vacancies are likely to form at clusters of Mn cations. Charge localized in the immediate vicinity of the vacancy has a low activation barrier for transporting between both equivalent (in-plane) positions as well as non-equivalent (out-of-plane) positions. Excess charge localized in the cell is affected significantly by the presence of the vacancy, showing an increase of ~0.1 eV in the activation barrier as compared with transport in the pristine cell. The increase in the activation barrier for excess charge transport is found to be due to a concurrent transfer of charge adjacent to the vacancy, in a manner that maintains maximal distance between the excess charge and the vacancy-induced charge. These results provide insights into the effects of vacancies in high-order spinels and could help in tuning these materials' electronic properties, perhaps by inducing a preferred directionality for charge transport near the vacancy.

ASSOCIATED CONTENT

Supporting Information

The Supporting Information is available free of charge at https://pubs.acs.org/doi/10.1021/acsmaterialsau.1c00051.

Supporting results and computational unit cells (PDF)

https://doi.org/10.1021/acsmaterialsau.1c00051
ACS Mater. Au 2022, 2, 269−277

AUTHOR INFORMATION

Corresponding Author

Maytal Caspary Toroker − *Department of Materials Science and Engineering, Technion-Israel Institute of Technology, Haifa 3200003, Israel; The Nancy and Stephen Grand Technion Energy Program, Haifa 3200003, Israel;* orcid.org/0000-0003-1449-2977; Email: maytalc@technion.ac.il

Author

Roni Eppstein − *Department of Materials Science and Engineering, Technion-Israel Institute of Technology, Haifa 3200003, Israel*

Complete contact information is available at: https://pubs.acs.org/10.1021/acsmaterialsau.1c00051

Notes

The authors declare no competing financial interest.

ACKNOWLEDGMENTS

This research was supported by a grant from the United States-Israel Binational Science Foundation (BSF), Jerusalem, Israel, and the United States National Science Foundation (NSF). This research was supported by the Nancy and Stephen Grand Technion Energy Program (GTEP). This article is based upon work from COST Action 18234, supported by COST (European Cooperation in Science and Technology).

REFERENCES

(1) Fortunato, E.; Ginley, D.; Hosono, H.; Paine, D. C. Transparent Conducting Oxides for Photovoltaics. *MRS Bull.* **2007**, *32*, 242−247.

(2) Rühle, S.; Anderson, A. Y.; Barad, H.-N.; Kupfer, B.; Bouhadana, Y.; Rosh-Hodesh, E.; Zaban, A. All-Oxide Photovoltaics. *J. Phys. Chem. Lett.* **2012**, *3*, 3755−3764.

(3) Grinberg, I.; West, D. V.; Torres, M.; Gou, G.; Stein, D. M.; Wu, L.; Chen, G.; Gallo, E. M.; Akbashev, A. R.; Davies, P. K.; Spanier, J. E.; Rappe, A. M. Perovskite Oxides for Visible-Light-Absorbing Ferroelectric and Photovoltaic Materials. *Nature* **2013**, *503*, 509−512.

(4) Ormerod, R. M. Solid Oxide Fuel Cells. *Chem. Soc. Rev.* **2003**, *32*, 17−28.

(5) Brett, D. J.; Atkinson, A.; P. Brandon, N.; J. Skinner, S. Intermediate Temperature Solid Oxide Fuel Cells. *Chem. Soc. Rev.* **2008**, *37*, 1568−1578.

(6) Jacobson, A. J. Materials for Solid Oxide Fuel Cells. *Chem. Mater.* **2010**, *22*, 660−674.

(7) Yang, J. J.; Pickett, M. D.; Li, X.; Ohlberg, D. A. A.; Stewart, D. R.; Williams, R. S. Memristive Switching Mechanism for Metal/Oxide/Metal Nanodevices. *Nat. Nanotechnol.* **2008**, *3*, 429−433.

(8) Kim, M.-G.; Kanatzidis, M. G.; Facchetti, A.; Marks, T. J. Low-Temperature Fabrication of High-Performance Metal Oxide Thin-Film Electronics via Combustion Processing. *Nat. Mater.* **2011**, *10*, 382−388.

(9) Yu, S.; Wu, Y.; Jeyasingh, R.; Kuzum, D.; Wong, H.-S. P. An Electronic Synapse Device Based on Metal Oxide Resistive Switching Memory for Neuromorphic Computation. *IEEE Trans. Electron Devices* **2011**, *58*, 2729−2737.

(10) Bibes, M.; Barthelemy, A. Oxide Spintronics. *IEEE Trans. Electron Devices* **2007**, *54*, 1003−1023.

(11) Opel, M. Spintronic Oxides Grown by Laser-MBE. *J. Phys. D: Appl. Phys.* **2011**, *45*, No. 033001.

(12) Holstein, T. Studies of Polaron Motion: Part II. The "Small" Polaron. *Ann. Phys.* **1959**, *8*, 343−389.

(13) Reticcioli, M.; Diebold, U.; Kresse, G.; Franchini, C. Small Polarons in Transition Metal Oxides. In *Handbook of Materials Modeling: Applications: Current and Emerging Materials*; Andreoni, W.; Yip, S., Eds.; Springer International Publishing: Cham, 2019; pp 1−39.

(14) Austin, I. G.; Mott, N. F. Polarons in Crystalline and Non-Crystalline Materials. *Adv. Phys.* **1969**, *18*, 41−102.

(15) Bhargava, A.; Chen, C. Y.; Dhaka, K.; Yao, Y.; Nelson, A.; Finkelstein, K. D.; Pollock, C. J.; Caspary Toroker, M.; Robinson, R. D. Mn Cations Control Electronic Transport in Spinel $Co_xMn_{3-x}O_4$ Nanoparticles. *Chem. Mater.* **2019**, *31*, 4228−4233.

(16) Bhargava, A.; Eppstein, R.; Sun, J.; Smeaton, M. A.; Paik, H.; Kourkoutis, L. F.; Schlom, D. G.; Toroker, M. C.; Robinson, R. D. Breakdown of the Small-Polaron Hopping Model in Higher-Order Spinels. *Adv. Mater.* **2020**, *32*, No. 2004490.

(17) Ndione, P. F.; Shi, Y.; Stevanovic, V.; Lany, S.; Zakutayev, A.; Parilla, P. A.; Perkins, J. D.; Berry, J. J.; Ginley, D. S.; Toney, M. F. Control of the Electrical Properties in Spinel Oxides by Manipulating the Cation Disorder. *Adv. Funct. Mater.* **2014**, *24*, 610−618.

(18) Tuller, H. L.; Bishop, S. R. Point Defects in Oxides: Tailoring Materials Through Defect Engineering. *Annu. Rev. Mater. Res.* **2011**, *41*, 369−398.

(19) Hu, J.; Zhao, X.; Chen, W.; Chen, Z. Enhanced Charge Transport and Increased Active Sites on α-Fe_2O_3 (110) Nanorod Surface Containing Oxygen Vacancies for Improved Solar Water Oxidation Performance. *ACS Omega* **2018**, *3*, 14973−14980.

(20) Kerisit, S.; Rosso, K. M. Charge Transfer in FeO: A Combined Molecular-Dynamics and Ab Initio Study. *J. Chem. Phys.* **2005**, *123*, No. 224712.

(21) Toroker, M. C.; Carter, E. A. Hole Transport in Non-stoichiometric and Doped Wüstite. *J. Phys. Chem. C* **2012**, *116*, 17403−17413.

(22) Muhich, C. L.; Ehrhart, B. D.; Witte, V. A.; Miller, S. L.; Coker, E. N.; Musgrave, C. B.; Weimer, A. W. Predicting the Solar Thermochemical Water Splitting Ability and Reaction Mechanism of Metal Oxides: A Case Study of the Hercynite Family of Water Splitting Cycles. *Energy Environ. Sci.* **2015**, *8*, 3687−3699.

(23) Trottier, R. M.; Bare, Z. J. L.; Millican, S. L.; Musgrave, C. B. Predicting Spinel Disorder and Its Effect on Oxygen Transport Kinetics in Hercynite. *ACS Appl. Mater. Interfaces* **2020**, *12*, 23831−23843.

(24) Song, J.; Shin, D. W.; Lu, Y.; Amos, C. D.; Manthiram, A.; Goodenough, J. B. Role of Oxygen Vacancies on the Performance of $Li[Ni_{0.5-x}Mn_{1.5+x}]O_4$ (x = 0, 0.05, and 0.08) Spinel Cathodes for Lithium-Ion Batteries. *Chem. Mater.* **2012**, *24*, 3101−3109.

(25) Lim, D.; Kong, H.; Lim, C.; Kim, N.; Shim, S. E.; Baeck, S.-H. Spinel-Type $NiCo_2O_4$ with Abundant Oxygen Vacancies as a High-Performance Catalyst for the Oxygen Reduction Reaction. *Int. J. Hydrogen Energy* **2019**, *44*, 23775−23783.

(26) Hohenberg, P.; Kohn, W. Inhomogeneous Electron Gas. *Phys. Rev.* **1964**, *136*, B864−B871.

(27) Kohn, W.; Sham, L. J. Self-Consistent Equations Including Exchange and Correlation Effects. *Phys. Rev.* **1965**, *140*, A1133−A1138.

(28) Perdew, J. P.; Burke, K.; Ernzerhof, M. Generalized Gradient Approximation Made Simple. *Phys. Rev. Lett.* **1996**, *77*, 3865−3868.

(29) Blöchl, P. E. Projector Augmented-Wave Method. *Phys. Rev. B* **1994**, *50*, 17953−17979.

(30) Kresse, G.; Joubert, D. From Ultrasoft Pseudopotentials to the Projector Augmented-Wave Method. *Phys. Rev. B* **1999**, *59*, 1758−1775.

(31) Dudarev, S. L.; Botton, G. A.; Savrasov, S. Y.; Humphreys, C. J.; Sutton, A. P. Electron-Energy-Loss Spectra and the Structural Stability of Nickel Oxide: An LSDA+U Study. *Phys. Rev. B* **1998**, *57*, 1505−1509.

(32) Huang, J. R.; Cheng, C. Cation and Magnetic Orders in $MnFe_2O_4$ from Density Functional Calculations. *J. Appl. Phys.* **2013**, *113*, No. 033912.

(33) Kanan, D. K.; Carter, E. A. Band Gap Engineering of MnO via ZnO Alloying: A Potential New Visible-Light Photocatalyst. *J. Phys. Chem. C* **2012**, *116*, 9876−9887.

(34) Momma, K.; Izumi, F. VESTA 3 for Three-Dimensional Visualization of Crystal, Volumetric and Morphology Data. *J. Appl. Crystallogr.* **2011**, *44*, 1272−1276.
(35) Dorris, S. E. The Electrical Properties and Cation Distributions of the Fe_3O_4-Mn_3O_4 Solid Solution. Ph.D. Thesis, Northwestern University: Evanston, IL, USA, 1986.
(36) Néel, M. L. Propriétés magnétiques des ferrites; ferrimagnétisme et antiferromagnétisme. *Ann. Phys.* **1948**, *12*, 137−198.
(37) Shull, C. G.; Wollan, E. O.; Koehler, W. C. Neutron Scattering and Polarization by Ferromagnetic Materials. *Phys. Rev.* **1951**, *84*, 912−921.
(38) Hastings, J. M.; Corliss, L. M. Neutron Diffraction Study of Manganese Ferrite. *Phys. Rev.* **1956**, *104*, 328−331.
(39) Singh, D. J.; Gupta, M.; Gupta, R. Magnetism and Electronic Structure in $ZnFe_2O_4$ and $MnFe_2O_4$. *J. Appl. Phys.* **2002**, *91*, 7370−7372.
(40) Elfalaky, A.; Soliman, S. Theoretical Investigation of $MnFe_2O_4$. *J. Alloys Compd.* **2013**, *580*, 401−406.
(41) Santos-Carballal, D.; Roldan, A.; Grau-Crespo, R.; de Leeuw, N. H. First-Principles Study of the Inversion Thermodynamics and Electronic Structure of FeM_2X_4 (Thio)Spinels (M = Cr, Mn, Co, Ni; X = O, S). *Phys. Rev. B* **2015**, *91*, No. 195106.
(42) Brabers, V. A. M.; Klerk, J. The Infrared Absorption Spectrum and the Inversion Degree of Manganese Ferrite. *Solid State Commun.* **1974**, *14*, 613−615.
(43) Boucher, B.; Buhl, R.; Perrin, M. Magnetic Structure of Iron Manganite by Neutron Diffraction. *J. Appl. Phys.* **1969**, *40*, 1126−1127.
(44) Bader, R. F. W. *Atoms in Molecules: A Quantum Theory; International Series of Monographs on Chemistry*; Oxford University Press: Oxford, New York, 1994.
(45) Henkelman, G.; Arnaldsson, A.; Jónsson, H. A Fast and Robust Algorithm for Bader Decomposition of Charge Density. *Comput. Mater. Sci.* **2006**, *36*, 354−360.
(46) Sanville, E.; Kenny, S. D.; Smith, R.; Henkelman, G. Improved Grid-Based Algorithm for Bader Charge Allocation. *J. Comput. Chem.* **2007**, *28*, 899−908.
(47) Tang, W.; Sanville, E.; Henkelman, G. A Grid-Based Bader Analysis Algorithm without Lattice Bias. *J. Phys.: Condens. Matter* **2009**, *21*, No. 084204.
(48) Yu, M.; Trinkle, D. R. Accurate and Efficient Algorithm for Bader Charge Integration. *J. Chem. Phys.* **2011**, *134*, No. 064111.
(49) Marcus, R. A. On the Theory of Oxidation-Reduction Reactions Involving Electron Transfer. I. *J. Chem. Phys.* **1956**, *24*, 966−978.
(50) Marcus, R. A.; Sutin, N. Electron Transfers in Chemistry and Biology. *Biochim. Biophys. Acta, Rev. Bioenerg.* **1985**, *811*, 265−322.
(51) Deskins, N. A.; Dupuis, M. Electron Transport via Polaron Hopping in Bulk TiO_2: A Density Functional Theory Characterization. *Phys. Rev. B* **2007**, *75*, No. 195212.
(52) Wang, Z.; Bevan, K. H. Exploring the Impact of Semicore Level Electronic Relaxation on Polaron Dynamics: An Adiabatic Ab Initio Study of $FePO_4$. *Phys. Rev. B* **2016**, *93*, No. 024303.
(53) Shiiba, H.; Zettsu, N.; Nakayama, M.; Oishi, S.; Teshima, K. Defect Formation Energy in Spinel $LiNi_{0.5}Mn_{1.5}O_{4-\delta}$ Using Ab Initio DFT Calculations. *J. Phys. Chem. C* **2015**, *119*, 9117−9124.
(54) Lai, F.; Feng, J.; Ye, X.; Zong, W.; He, G.; Yang, C.; Wang, W.; Miao, Y.-E.; Pan, B.; Yan, W.; Liu, T.; Parkin, I. Oxygen Vacancy Engineering in Spinel-Structured Nanosheet Wrapped Hollow Polyhedra for Electrochemical Nitrogen Fixation under Ambient Conditions. *J. Mater. Chem. A* **2020**, *8*, 1652−1659.
(55) Shi, X.; Bernasek, S. L.; Selloni, A. Formation, Electronic Structure, and Defects of Ni Substituted Spinel Cobalt Oxide: A DFT +U Study. *J. Phys. Chem. C* **2016**, *120*, 14892−14898.
(56) Liu, F.; Dai, J.; Liu, J.; Yang, Y.; Fang, R. Density Functional Theory Study on the Reaction Mechanism of Spinel $CoFe_2O_4$ with CO during Chemical-Looping Combustion. *J. Phys. Chem. C* **2019**, *123*, 17335−17342.
(57) Bhattacharjee, S.; Banerjee, A.; Mazumder, N.; Chanda, K.; Sarkar, S.; Kumar Chattopadhyay, K. Negative Capacitance Switching in Size-Modulated Fe_3O_4 Nanoparticles with Spontaneous Non-Stoichiometry: Confronting Its Generalized Origin in Non-Ferroelectric Materials. *Nanoscale* **2020**, *12*, 1528−1540.
(58) Feng, Y.; Wang, N.; Guo, X. Density Functional Theory Study on Improved Reactivity of Alkali-Doped Fe_2O_3 Oxygen Carriers for Chemical Looping Hydrogen Production. *Fuel* **2019**, *236*, 1057−1064.
(59) Jian, Y.; Yu, T.; Jiang, Z.; Yu, Y.; Douthwaite, M.; Liu, J.; Albilali, R.; He, C. In-Depth Understanding of the Morphology Effect of α-Fe_2O_3 on Catalytic Ethane Destruction. *ACS Appl. Mater. Interfaces* **2019**, *11*, 11369−11383.
(60) Jian, W.; Wang, S.-P.; Zhang, H.-X.; Bai, F.-Q. Disentangling the Role of Oxygen Vacancies on the Surface of Fe_3O_4 and γ-Fe_2O_3. *Inorg. Chem. Front.* **2019**, *6*, 2660−2666.
(61) Ritzmann, A. M.; Pavone, M.; Muñoz-García, A. B.; Keith, J. A.; Carter, E. A. *Ab Initio* DFT+*U* Analysis of Oxygen Transport in $LaCoO_3$: the Effect of Co^{3+} Magnetic States. *J. Mater. Chem. A* **2014**, *2*, 8060−8074.
(62) Liu, H.; Di Valentin, C. Band Gap in Magnetite above Verwey Temperature Induced by Symmetry Breaking. *J. Phys. Chem. C* **2017**, *121*, 25736−25742.
(63) Pavone, M.; Ritzmann, A. M.; Carter, E. A. Quantum-Mechanics-Based Design Principles for Solid Oxide Fuel Cell Cathode Materials. *Energy Environ. Sci.* **2011**, *4*, 4933−4937.

https://doi.org/10.1021/acsmaterialsau.1c00051
ACS Mater. Au 2022, 2, 269−277